ADVANCED FUNCTIONAL MATERIALS

www.afm-journal.de

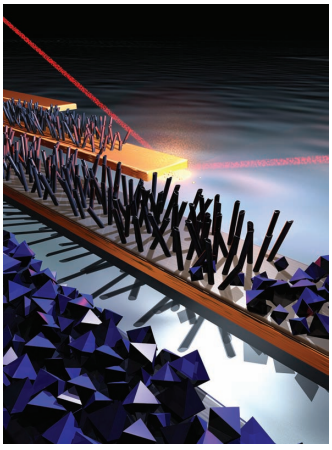

Porous Materials

Controlling metal–organic framework (MOF) growth on different substrates is crucial for device fabrication. An Australian–Japanese collaboration between M. Takahashi, P. Falcaro, and co-workers demonstrates on page 1969 how MOF coatings on flat plates, 3D surfaces, and patterns can be fabricated using a facile, two-step conversion process at room temperature with aqueous/alocholic solutions. Using copper substrates, nanotubes are grown and then quickly converted to MOF crystals, and MOF patterns are fabricated using sunlight.

Nanoparticles

Luminescent ZnO quantum dots are prepared by G. Bacher, U. Kortshagen, and co-workers in a nonthermal plasma reactor operated with a high frequency source. Quantum dots with diameters down to 2.1 nm are achieved, exhibiting exceptional quantum yields of up to 60%. On page 1988, the mechanism for the dominating green–yellow emission is discussed and the influence of oxygen species on the emission spectrum is investigated.

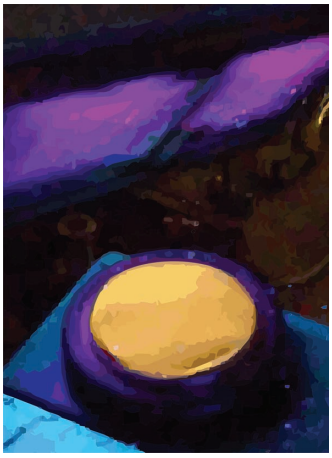

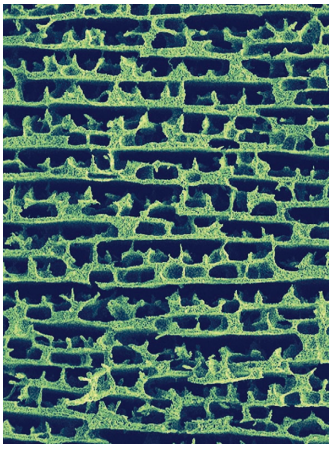

Porous Scaffolds

This image was created by freeze casting TiO_2 powders, using ice as a template to control the architectural morphology of the scaffold. Such bioinspired scaffolds with equal porosity but different pore architectures exhibit compressive mechanical properties that change as a function of the pore morphology. On page 1978, the ceramic scaffolds are prepared by M. M. Porter et al. by freeze casting aqueous slurries with different soluble additives to alter the viscosity, pH, or alcohol concentration.

FULL PAPERS

Porous Materials

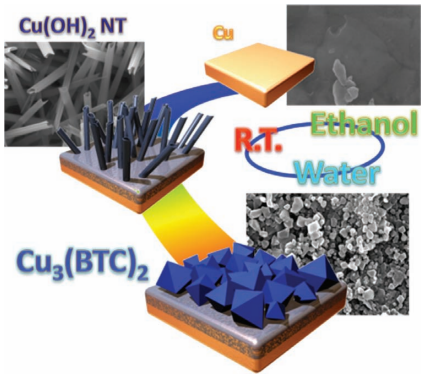

HKUST-1 [$Cu_3(BTC)_2$] coatings with a good adhesion are homogeneously fabricated on copper metal plates, 3D objects, and patterns. The metal organic-frameworks (MOFs) are converted from any metallic Cu object via $Cu(OH)_2$ nanotubes at room temperature in approximately 30 min using an aqueous ethanolic mixture. The conversion mechanism from copper hydroxide nanotubes into $Cu_3(BTC)_2$ is revealed by electron microscopy time-course monitoring.

Porous Scaffolds

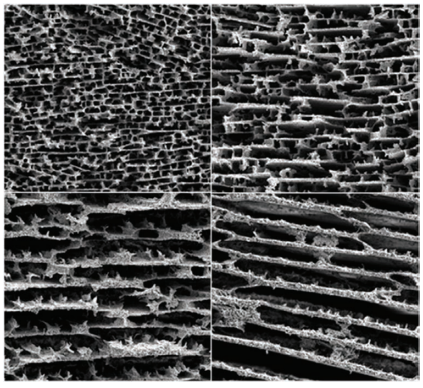

Bioinspired scaffolds with equal porosity, but different pore architectures exhibit compressive mechanical properties that change as a function of the pore morphology. The scaffolds are fabricated by freeze casting with different soluble additives to alter the viscosity, pH, or alcohol concentration. A simplified Euler buckling analysis predicts the strength of the scaffolds as a function of the pore aspect ratio.

Nanoparticles

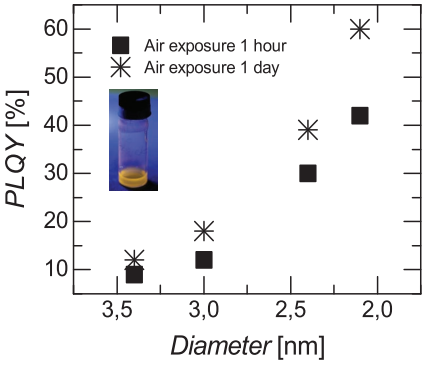

ZnO quantum dots are prepared in a nonthermal plasma reactor operated with a high frequency source. Quantum dots with diameters down to 2.1 nm are achieved, exhibiting exceptional high quantum yields up to 60%. The mechanism for the dominating green–yellow emission is discussed and the influence of oxygen species on the emission spectrum is investigated.

Organic Electronics

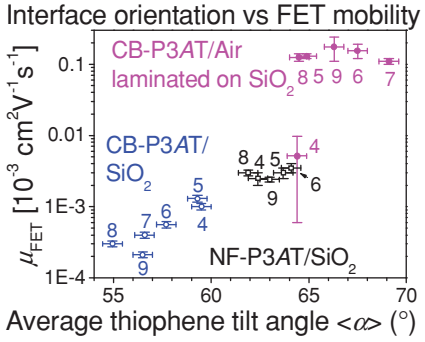

The orientation and organization of semiconducting polymer at the polymer/(gate dielectric) interface has a strong influence on OFET hole mobilities. For poly(3-alkylthiophene) thin films, both from chlorobenzene and from nanofiber dispersions, orientation and OFET mobility are compared for the interfaces formed at bare SiO_2 and at air (then laminated on bare SiO_2), that is, at two extremes of the polarity scale.

FULL PAPERS

An effective way of using ionic liquid as a gate dielectric as well as a pressure medium is presented to tune the transport of an exemplary polymer semiconductor, poly(2,5-bis(3-tetradecylthiophene-2-yl)thieno[3,2-b]thiophene) (pBTTT-C14). By combining both gating and pressuring, the room temperature conductivity of the polymer film is dramatically enhanced and a crossover of transport properties is observed from one-dimensional to three-dimensional hopping at low temperatures.

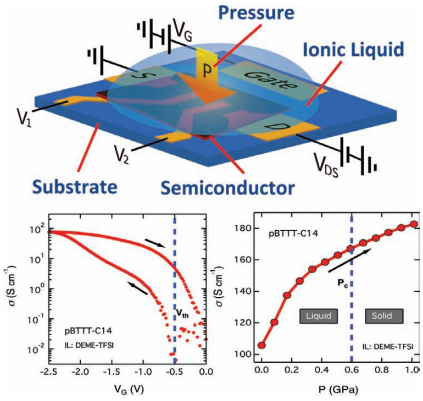

Conjugated Polymers

Transport Properties of Polymer Semiconductor Controlled by Ionic Liquid as a Gate Dielectric and a Pressure Medium

Ordered mesoporous carbon is proposed to be directly coated on 3D graphene foam. After further coating with 1D silver nanowires, the obtained Ag NWs/3D-graphene foam/OMC (Ag-GF-OMC) exhibits exceptional electrical conductivity (up to 762 S cm^{-1}) and mechanical robustness. As a result, it can act as a new type of flexible electrode for high performance supercapacitors.

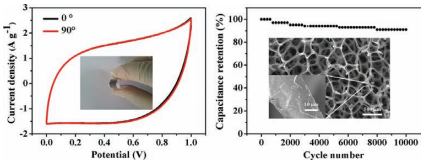

Nanowires

Highly Conductive Ordered Mesoporous Carbon Based Electrodes Decorated by 3D Graphene and 1D Silver Nanowire for Flexible Supercapacitor

Highly active Pd nanoparticles are deposited on the surface of magnetic Co/C nanobeads by microwave heating. The hybrid material is applied in the hydrogenation of alkenes exhibiting turnover frequencies up to 11 095 h^{-1}, exceeding Pd@CNT and Pd/C catalysts. The high magnetization of the core enables rapid separation and recycling of the material with negligible Pd leaching detected for each cycle.

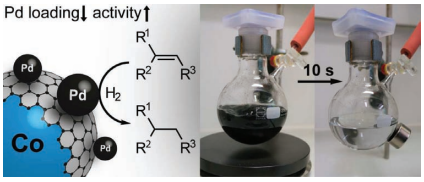

Hybrid Nanomaterials

Palladium Nanoparticles Supported on Magnetic Carbon-Coated Cobalt Nanobeads: Highly Active and Recyclable Catalysts for Alkene Hydrogenation

A prestrain strategy is introduced as a means for enhancing the stretchability of for serpentine metal interconnect structures bonded to soft elastomers. Systematic studies of the buckling physics include results from analytical models, finite element method computations, and quantitative experiments. The results have general utility for future work in stretchable inorganic device systems.

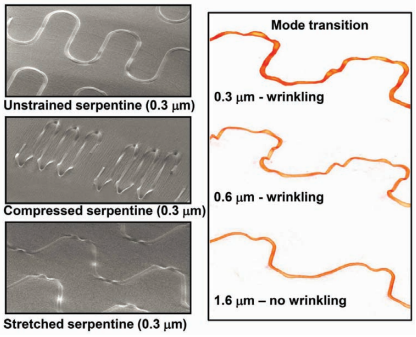

Flexible Electronics

Experimental and Theoretical Studies of Serpentine Microstructures Bonded To Prestrained Elastomers for Stretchable Electronics

FULL PAPERS

Thin Films

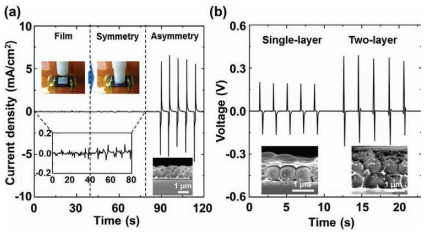

For the first time, high-performance pressure sensors and piezoelectric nanogenerators based on embossed hollow hemispheres are reported. The pressure sensor with the asymmetric hemispheres results in level at about 7 mA cm^{-2} at normal force of 30 N. The nanogenerators generate the voltage output of ≈0.2 V, and demonstrate enhanced output voltage up to 2 times through a layer-by-layer stacking.

Li-Ion Batteries

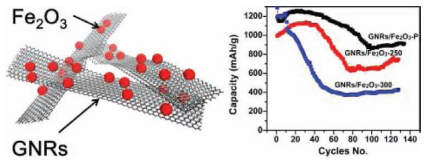

A facile and scalable synthesis route to a graphene nanoribbon (GNR)/Fe_2O_3 composite is developed as an anode material for lithium-ion batteries. The unique structures of the GNRs with high electrical conductivity and the enhanced vacancy of the iron oxide nanoparticles leads to excellent electrochemical performance. The fabricated anode shows a reversible capacity of 1190 mAh/g and retains 910 mAh/g after 134 cycles with a high rate performance of 544 mAh/g at a rate of 2 A/g.

Alloy Nanoparticles

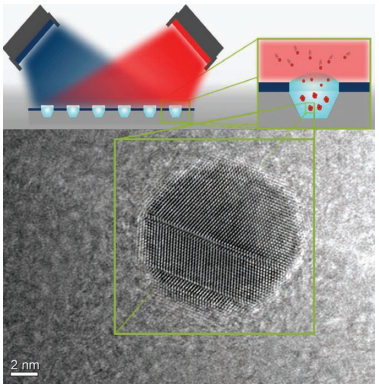

Materials libraries of Au–Cu alloy nanoparticles (NPs) synthesized by combinatorial co-sputter deposition of Cu and Au into the ionic liquid (IL) $[C_1C_4im][Tf_2N]$ are investigated by TEM, XRD, UV-Vis, and ATR-FTIR spectroscopy. A new NP isolation process is developed enabling separation of NPs from IL without changing size, morphology, composition, and aggregation state.

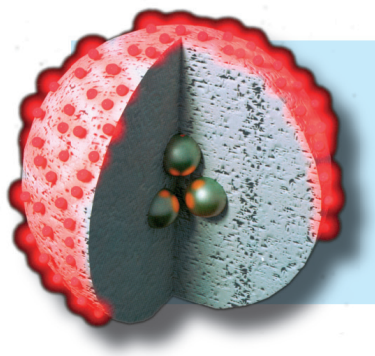

How to contact us:

Editorial Office:
Phone: (+49) 6201-606-286/531
Fax: (+49) 6201-606-500
Email: afm@wiley-vch.de

Reprints:
cherth@wiley-vch.de

Copyright Permission:
Fax: (+49) 6201-606-332
Email: rights@wiley-vch.de

FULL PAPERS

Transistors

Solution-Processed Small-Molecule Bulk Heterojunction Ambipolar Transistors

Solution-processed small-molecule bulk heterojunction (BHJ) ambipolar organic thin-film transistors fabricated by blending two p-channel benzo[d,d′]thieno[3,2-b;4,5-b′]dithiophene (BTDT) derivatives with n-channel C_{60} result in balanced hole and electron carrier mobilities. A complementary-like inverter composed of two ambipolar thin-film transistors with a gain of 115 is achieved.

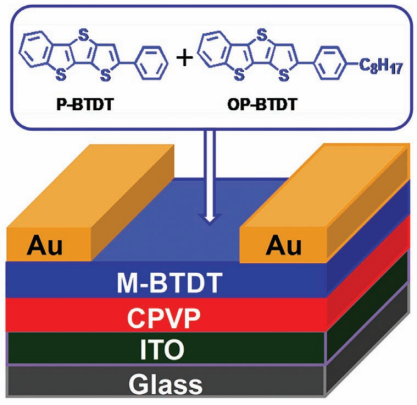

OLEDs

Bisanthracene-Based Donor–Acceptor-type Light-Emitting Dopants: Highly Efficient Deep-Blue Emission in Organic Light-Emitting Devices

Donor–accepotor (DA)-type deep-blue fluorescent compounds are synthesized. Twisted conformations of the two anthracene units in the compounds effectively prevent π-conjugation. The compounds show deep-blue photoluminescence (PL) with a high quantum efficiency, almost independent of solvent polarity. The weak DA-type compound exhibits an external quantum efficiency >10% and deep-blue emission with CIE (0.15, 0.06) in a light-emitting device.

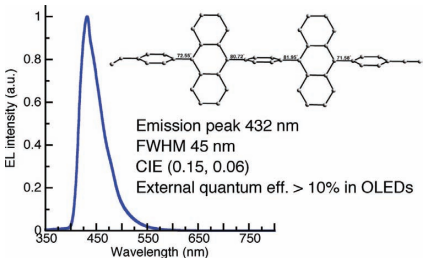

Graphene

Shape Control of Mn_3O_4 Nanoparticles on Nitrogen-Doped Graphene for Enhanced Oxygen Reduction Activity

Sphere, cube, and ellipsoid-like Mn_3O_4 nanoparticles integrated with nitrogen-doped graphene are synthesized and used as oxygen reduction reaction (ORR) catalysts. The catalyst shape dependence on the ORR activity is investigated, and the hybrid of ellipsoidal Mn_3O_4/N-graphene exhibits the best ORR activity, which may be related to the dominant (001) facets in Mn_3O_4 nanocrystals.

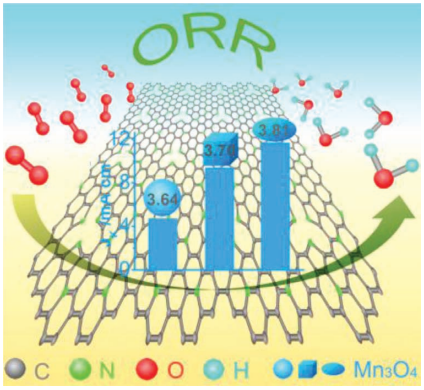

Protein Sensors

M13 Bacteriophage as Materials for Amplified Surface Enhanced Raman Scattering Protein Sensing

Protein sensing design based on M13 bacteriophage and Raman active core–shell nanoparticles. M13 bacteriophage can be utilized as a biomaterial scaffold for generating an amplified signal. The layer by layer deposition of unique Raman active nanoparticles on the phage produced exponential gains in Raman signal compared to that of antibodies at the same antigen concentration.

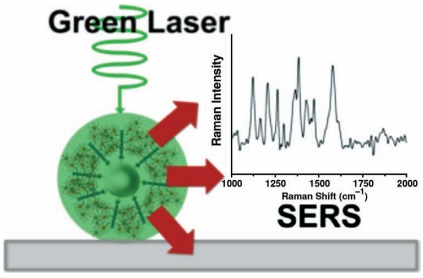

FULL PAPERS

Pathogen Attachment

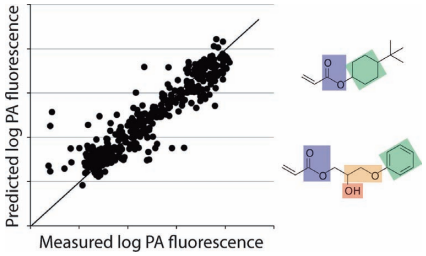

Data from polymer microarrays exposed to three clinical pathogens are used to derive robust and predictive machine-learning models of pathogen attachment. The model could predict pathogen attachment quantitatively, predict attachment of new polymers, and identify polymer surface functional groups that enhance or diminish pathogen attachment.

Semiconductors

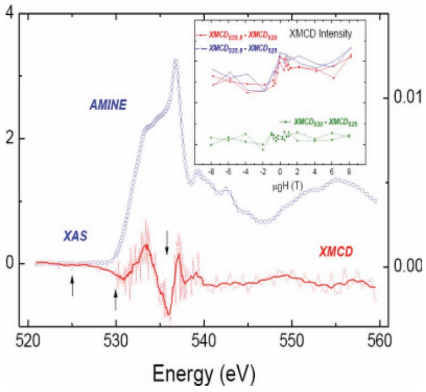

X-ray magnetic circular dichroism spectroscopy (XMCD) recorded at the O K-edge demonstrates the intrinsic occurrence of room temperature ferromagnetism (RTFM) in ZnO-based nanoscaled materials and the occurrence of an oxygen ferromagnetic state in the absence of magnetic atoms.

Lithium-Air Batteries

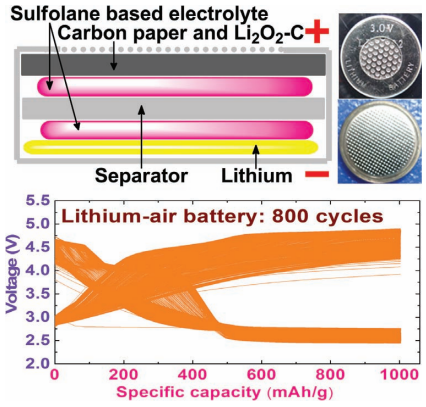

By optimizing the battery formula, including solvents, salts, current collector, and positive electrode materials, a lithium-air battery can operate 800 cycles with a specific capacity of 1000 mAh g^{-1}. The findings described here are expected to benefit the pursuit of green, sustainable, and high-performance lithium-air batteries.